Spatial modulation of individual behaviors enables collective decision-making during bacterial group migration

Yang BAI[1*], Caiyun HE[1,2*], Junjiajia Long[3], Xuefei Li[1,2], Xiongfei FU[1,2+]

[1]Guangdong Provincial Key Laboratory of Synthetic Genomics, CAS Key Laboratory for Quantitative Engineering Biology, Shenzhen Institute of Synthetic Biology, Shenzhen Institutes of Advanced Technology, Chinese Academy of Sciences, Shenzhen, 518055, China

[2]University of Chinese Academy of Sciences, Beijing, 100049, China

[3]Yale University, Department of Physics, New Haven, CT 06520-8120, USA

*Yang BAI & Caiyun HE contributed equally to this work.

+To whom correspondence should be addressed

Email: xiongfei.fu@siat.ac.cn

Abstract

Coordination of individuals with diversity often requires sophisticated communications and high-order computational abilities. Microbial populations can exhibit diverse individualistic behaviors and yet can engage in collective migratory patterns with a spatially sorted arrangement of phenotypes following a self-generated attractant gradient. However, it's unclear how individual bacteria without complex computational abilities can achieve the consistent group performance and determine their positions in the group while facing spatiotemporally dynamic stimuli. Here, we investigate the statistics of bacterial run-and-tumble trajectories during group migration. We discover that, despite of the constant migrating speed as a group, the individual drift velocity exhibits a spatially dependent structure that decreases from the back to the front of the group. The spatial modulation of individual stochastic behaviors constrains cells in the group, ensuring the coherent population movement with ordered patterns of phenotypes. These results reveal a simple computational principle for emergent collective behaviors from heterogeneous individuals.

Introduction

Collective group migration as an important class of coordinated behaviors is ubiquitous in living systems, such as navigation, foraging, and range expansion (Krause, Ruxton et al., 2002, Partridge, 1982, Sumpter, 2010). In the presence of individual heterogeneity, the migrating group often exhibit spatially ordered arrangements of phenotypes (Krause et al., 2002, Parrish & Edelstein-Keshet, 1999, Partridge, 1982, Sumpter, 2010). In animal group migration, individual behavioral abilities (e.g. directional-sensitive) would result social hierarchy, which further drives the spatial arrangement in coordinated group (Couzin, Krause et al., 2005). At the same time, the spatial arrangements can lead to different costs and benefits for the individuals participating in the group migration (Krause, 1994, Parrish & Edelstein-Keshet, 1999, Partridge, 1982). Participating individuals must follow disciplinary rules to organize themselves into coordinated patterns while on the move, which requires complex computational abilities to interact with the group and the environment (Couzin & Krause, 2003, Couzin, Krausew et al., 2002, Vicsek & Zafeiris, 2012). Therefore, understanding how individuals of different phenotypes determine their group positions is an essential prerequisite to uncover the organization principles of collective populations.

The chemotactic microbe, *E. coli*, provides a simple model to address the emergence of collective decision-making, as it can both exhibit individualistic behaviors (Dufour, Gillet et al., 2016, Frankel, Pontius et al., 2014, Kussell & Leibler, 2005, Waite, Frankel et al., 2016, Waite, Frankel et al., 2018) and collective migratory patterns (Adler, 1966a, Fu, Kato et al., 2018, Keller & Segel, 1971, Wolfe & Berg, 1989). Individual cells perform run-and-tumble random motions by spontaneous switching the rotating direction of flagella (Berg, 2004, Berg & Brown, 1972). The cell can facilitate the chemotaxis pathway to control the switching frequency to bias in its favorable directions towards the chemoattractant gradient, where the efficiency to climb the gradient is defined as chemotactic ability (χ) (Celani & Vergassola, 2010, de Gennes, 2004, Dufour, Fu et al., 2014, Si, Wu et al., 2012). In addition, substantial phenotypic heterogeneity in chemotactic ability has been observed even for clonal bacterial population, which diversifies the chemotactic response of cells to identical signals (Spudich & Koshland, 1976, Waite et al., 2016, Waite et al., 2018). At the same time, despite of the stochastic solitary behavior and variations in phenotypic ability, *E. coli* population can migrate as a coherent group by following a self-generated attractant gradient (via consumption) (Adler, 1966a, Saragosti, Calvez et al., 2011, Wolfe & Berg, 1989). The group moving at a constant speed form a stable pattern of phenotypes sorted by their chemotactic abilities (Fig 1A), so as to maintain phenotypic diversity in the coherent migratory group (Fu et al., 2018, Waite et al., 2018). Intriguingly, it's believed that there are no direct communications among cells within such coordinated migration group (Cremer, Honda et al., 2019, Fu et al., 2018), and cells encounter highly dynamic external stimulus. How individuals with phenotypic and behavioral variations manage to

2

76   maintain the consistent group performance and determine their relative positions
77   in the group is still a mystery.

78   Here we analyzed bacterial trajectories in the chemotactic group migration using
79   a microfluidic system that enables us to simultaneously characterize the
80   quantitative properties of individual motions (see Materials and Methods). We
81   discovered that in the collectively migratory group, the run-and-tumble motions of
82   individual cells were spatially modulated to behave as mean-reverting processes
83   relative to the group, i.e. cells effectively tend to revert its direction of runs
84   towards the mean position of the group. The same rule of behavioral modulation
85   applies to cells of different phenotypes to allow them migrate at a consistent
86   average speed with an ordered spatial arrangement of phenotypes. By titrating
87   the phenotypes with different chemo-receptor abundance, we further
88   demonstrated that the mean-reversion rate of the behavioral modulation depends
89   on the sensitivity response to the chemoattractant gradient. Therefore, although
90   the high-order computational abilities are not available to the simple organisms,
91   the spatial modulation of stochastic behaviors at the individual level enables
92   novel decision-making capabilities at the population level.

Results

Spatially ordered bacteria behavior.

To directly investigate how bacteria with different chemotactic abilities determine their relative positions within the collective migration group via run-and-tumble random motions, we employed a Y-shape microfluidic device with a long channel of 20mm which allows us to generate a stable propagating band of bacteria as previously reported (Fu et al., 2018, Saragosti et al., 2011). Specifically, about 1.5×10^4 *E. coli* wild type cells (strain RP437) were loaded into the device, and the medium used is M9 motility buffer supplemented with 200μM aspartate (Asp) as the only chemo-attractant in the system (Adler, 1966b, Fu et al., 2018). Under this condition, only one dense band of migrating bacteria can be spontaneously formed (Fu et al., 2018), after the cells were centrifuged to the tip of the long channel. To quantify the statistics of the single-cell motions within the dense traveling band, we premixed a small fraction of bacteria (strain JCY1) which constitutively expresses yellow fluorescent protein with the non-fluorescent wild type population (strain RP437) by 1:400. The trajectories of fluorescent cells were then recorded under 4X objective with a frame rate of 9 fps for 10 mins (see Materials and Methods and Fig S1). As the fluorescent labeled cells show the same behavior as the wild type ones (Fig S1D), we can consider the behavior of fluorescent cells as the representatives in the migrating group (Fu et al., 2018, Saragosti et al., 2011).

As an important advantage of the experimental setup, we can trace the single cell motions within the dense band of group migration for long time (e.g. typical tracks are larger than 300 seconds) (Saragosti et al., 2011). Given the long trajectories of fluorescent bacteria, we first observed an overall trend of biased random motions of individual cells towards the group migration (Movie. S1). By analyzing the instantaneous velocity based on the trajectories of fluorescent bacteria projected to the group migration direction $x_i(t)$, we found that the average instantaneous velocity of the entire group, $V_G(t) = \langle \Delta x_i(t)/\Delta t \rangle$, kept constant over time, $V_G \sim 3.0 \, \mu m/s$, suggesting that the band of cells as a whole propagates at a constant speed (Fig S2). Consequently, in the moving coordinate ($z = x - V_G t$), the time-shifted cell density profiles $\rho(z)$ can be superimposed as an approximately invariant profile (Fig 1B). Furthermore, the average instantaneous velocity over the band profile, $V_I(z) = \langle \Delta x_i(z)/\Delta t \rangle$, remained the same as the group velocity ($V_G = \langle V_G(t) \rangle_t$) along the density profile (Fig 1B). We also verified that these observations did not depend on the sampling time interval (Fig S2). Therefore, despite of stochastic motions on single cell level, bacterial population are able to migrate as a stable group (Adler, 1966a, Fu et al., 2018, Saragosti et al., 2011).

133   Next, to address how the collective group movement emerge from the stochastic
134   solitary behavior, we analyzed the statistics of run-and-tumble events for
135   individual bacteria. Specifically, after identifying all the run states of individual
136   trajectories by a previously described computer assistant program (see Materials
137   and Methods) (Dufour et al., 2016, Waite et al., 2016), we aligned all the time-
138   shifted runs by their starting positions in the moving coordinate with respect to
139   the center of the group, and quantified the spatial distributions of the mean run
140   duration $\langle \tau_R(z) \rangle$, as well as the mean run length $\langle l_R(z) \rangle$. We find that both $\langle \tau_R(z) \rangle$
141   and $\langle l_R(z) \rangle$ increase from the back to the front of the moving group, while the
142   mean tumble time $\langle \tau_T(z) \rangle$ is almost invariant (Fig 1C). Note that previous
143   observations on the steady state profiles of population distribution exhibited that
144   phenotypes with low tumble bias would spontaneously position themselves in the
145   front of the migratory group (Fu et al., 2018). Besides the phenotypic distribution
146   along the wave profile, the spatial structure of run length/duration can also be
147   contributed by the modulation of bacterial behaviors in response to the
148   chemoattractant gradient (Dufour et al., 2014, Long, Zucker et al., 2017, Shimizu,
149   Tu et al., 2010). It's unclear how the individual behaviors are dynamically
150   modulated during the group migration.

151   To answer this question, we first investigated sample runs initiated from the back
152   (B), middle (M) and front (F) of the migration group. Qualitatively, the lengths of
153   representative runs in the front are longer but distribute more uniformly in terms
154   of the directionality, whereas the lengths of runs in the back are shorter but the
155   directions of runs are more likely pointing towards the direction of group
156   migration (Fig 1D). Quantitatively, the statistics of run lengths, as well as the run
157   durations, display exponential distributions, suggesting that the switch between
158   runs and tumbles follow Poisson process (Berg & Brown, 1972, Wang, Shi et al.,
159   2017) . Of those distributions, the means in the direction of group migration are
160   longer than that of the opposite direction (Fig 1E and Fig S3A). Furthermore, by
161   analyzing the angular distribution of the run length, we found that in the front of
162   the group, the difference between the forward runs and backward runs became
163   smaller despite increased mean values (Fig 1F). Moreover, we also observed
164   that the reorientation angles after tumble events exhibited a decreasing trend
165   along the wave profile (Fig S3E), suggesting a directional persistence towards
166   the group migration as previously reported (Saragosti et al., 2011). All these
167   results suggest that the bacteria in the back run more effectively towards the
168   group migration than those in the front.

169   To further quantify the efficiency of runs, we calculated the directional bias of run
170   length and run duration, which are defined as the ratio of the net run
171   length/duration in the direction of the group migration and run lengths/durations
172   in all directions, $B_l(z) \equiv \frac{\langle L_R(z) \cdot \cos \theta_R(z) \rangle}{\langle L_R(z) \rangle}$, and $B_\tau(z) \equiv \frac{\langle \tau_R(z) \cdot \cos \theta_R(z) \rangle}{\langle \tau_R(z) \rangle}$, respectively,
173   where θ_R is the angle between single runs and the migration direction. Both
174   quantities are spatially modulated as they decreased by 3~4 folds from the back

5

175 to the front of the migration group (Fig 1G), quantitatively indicating how much
176 more effectively the cells in the back behave than that in the front. As the tumble
177 duration is almost constant along the band profile (Fig 1C), we hypothesized that
178 the efficiency of runs would represent how fast that the cells climb the
179 chemoattractant gradient, suggesting that the spatial modulation in the directional
180 bias of runs enables cells in the back of the migration group to exhibit higher drift
181 velocity though the mean run length of them is shorter.
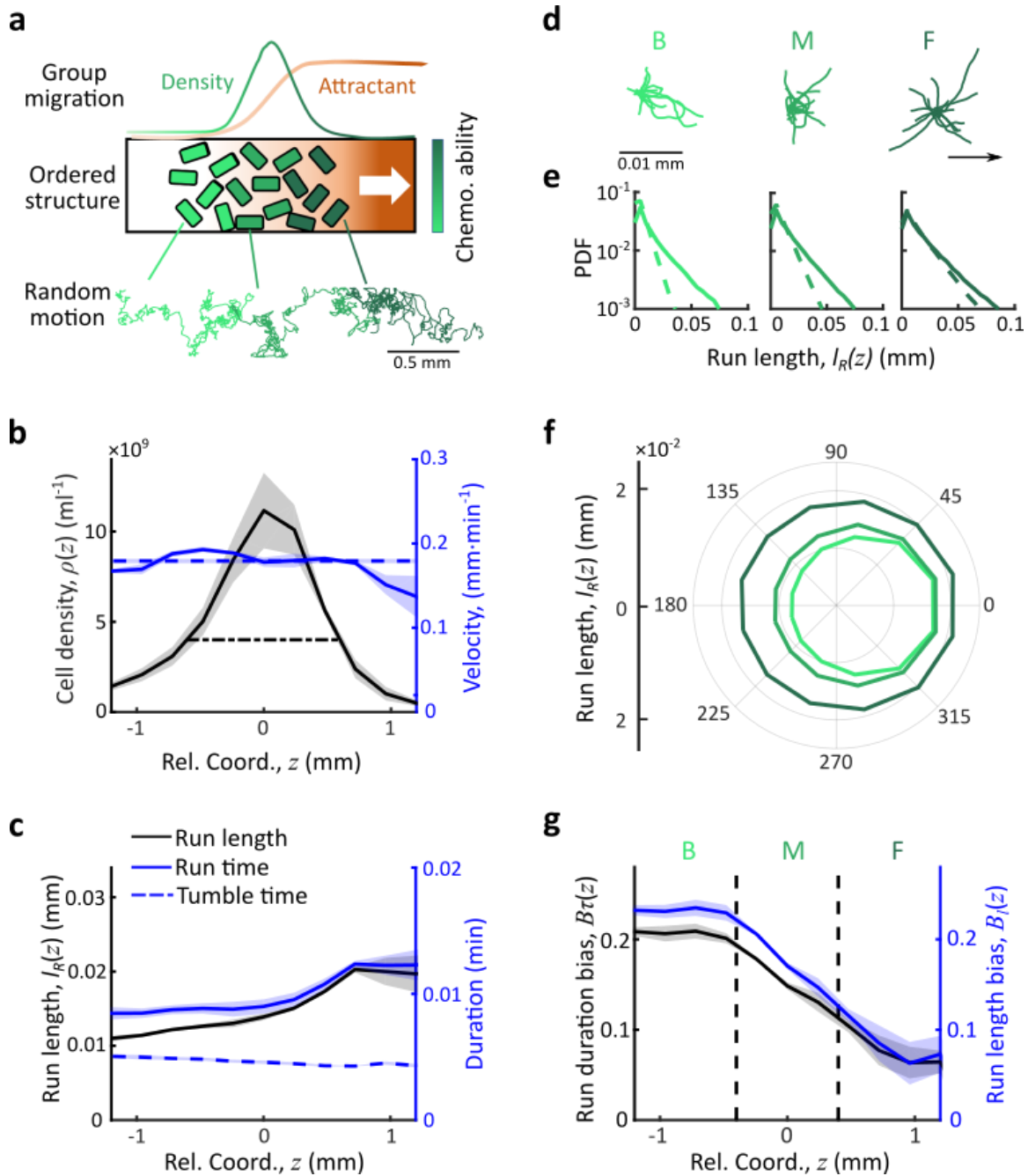
182

183 **Figure 1. Behavioral structure of individual bacteria in collective group**
184 **migration.**
185 (**A**) Illustration of bacterial chemotactic group migration. Bacteria may form
186 collective migrating group (green line) while consuming chemo-attractant
187 collectively (brown line). Bacterial population of diverse phenotypes are sorted by
188 their chemotactic abilities (increasing from light green to dark green) during
189 collective migration following the self-generated attractant gradient (brown color).
190 Meanwhile, as shown in the sample trajectories, individual cells perform run-and-
191 tumble random motions biased towards the group migration. (**B**) In the moving
192 coordinate $z = x - V_G t$, the bacteria density profile $\rho(z)$ is stable (black solid
193 line). The width of the density profile is defined as 2 times the standard deviation
194 of bacterial relative position (2σ, black dash line), represented by the black dash-
195 dotted line. The instantaneous velocity ($V_I(z)$) (blue solid line) is uniform and
196 equals to the average group velocity V_G (blue dash line). (**C**) The mean run length
197 $\langle l_R(z) \rangle$ (black solid line) and run time $\langle \tau_R(z) \rangle$ (blue solid line) increase from the
198 back (left) to front (right) of the migration group, while the mean tumble time
199 $\langle \tau_T(z) \rangle$ slightly decreases (blue dash line). (**D**) Sample runs of bacteria from the 3
200 regions. B, M, and F stands for the back, middle and front of the migration group,
201 respectively. Regions were defined by black dashed lines in *G*. Trajectories of
202 runs show that cells in the back of group tend to run forward, compared to cells in
203 other regions. (**E**) The exponential distribution of forward run length (solid lines)
204 and backward run length (dash lines) in 3 regions show that the difference of run
205 length between forward and backward for cells in the back is larger than cells in
206 other regions. (**F**) The mean run length in different directions, with the angular bin
207 size of 15°, also show that cells in the back were better skewed to run forward.
208 (**G**) The run length bias $B_l(z) = \frac{\langle l_R(z) \cdot \cos \theta_R(z) \rangle}{\langle l_R(z) \rangle}$ (black solid line) and the run time
209 bias $B_\tau(z) = \frac{\langle \tau_R(z) \cdot \cos \theta_R(z) \rangle}{\langle \tau_R(z) \rangle}$ (blue solid line) both decreased from the back to the
210 front of the migration group, which is also consistent with results shown in D-F. In
211 panel B, C, G, shaded area represents s.e.m. of 3 biological replicates. The
212 spatial bin size is $240 \mu m$.
213

Bacteria perform mean-reversion behavior as active particles in moving gradient.

To verify our hypothesis, we examined the expected drift velocity along the band profile, which is defined as the average projection of run length on the migration direction over the average duration of runs and tumbles, $V_D(z) \equiv \frac{\langle l_R(z) \cdot \cos\theta_R(z)\rangle}{\langle \tau_R(z)+\tau_T(z)\rangle}$ (Dufour et al., 2014). Unlike the spatially-uniform instantaneous velocity $V_I(z)$, the expected drift velocity $V_D(z)$ decreases linearly from the back to the front of the migration group with a fitted linear slope of $-r = -0.05\ \text{min}^{-1}$ (Fig 2A). The negative slope of $V_D(z)$ suggests a mean-reversion behavior of bacteria: the bacteria in the back of the migration group are expected to drift faster than the group ($V_D > V_G$), enabling the cells to catch up within the group, while the cells in the front are expected drift slower than the group ($V_D < V_G$), making the cells to slow down and fall back (Fig 2B). As another piece of evidence supporting the mean-reversion behavior, the time-shifted trajectories of cells relative to the group indicate that the cell motions perform sub-diffusive (Fig 2C), of which the mean square displacement (MSD) are constrained over time (Fig S3G). Thus, our observations indicate that the modulation of individual runs along the wave profile leads to the spatially-structured expected drift velocity, resulting an effective mean reversion process of cell motions.
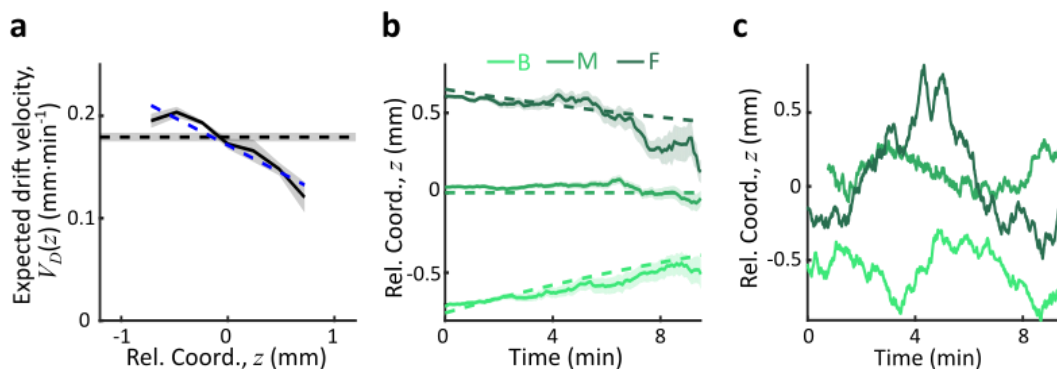
Figure 2. Mean-reversion behavior of individual bacteria relative to the group.

(**A**) The expected drift velocity $V_D = \frac{\langle l_R(z) \cdot \cos\theta_R(z)\rangle}{\langle \tau_R(z)+\tau_T(z)\rangle}$ (black solid line) decreases from the back to the front of the migration group. The blue dash line is the linear fit of the quantified experimental data, i.e., $V_D \approx -rz + V_{D0}$, with $r = 0.05 min^{-1}$ and $V_{D0} = 0.17 mm \cdot min^{-1}$. V_D crosses with the average group velocity V_G (black dash line), which implies that bacteria perform mean-reversion motions, i.e. cells in the back catch up the group while cells in the front lay back. The V_D curve and its linear fit was cut to present ~90% majority of cells ($\pm 1.65\sigma$). (**B**) The time evolution of the average expected position (z, solid lines) of cells starting from the back (light green), middle (green), and front (dark green) of the migration group (defined in Fig1. G). Shaded area represents s.e.m. of more than 450 cells

8

246 (see Methods). Analytically, the O-U type model predicts that $z = C_0 e^{-rt} -$
247 $(V_{D0} - V_G)/r$ (dash lines), where C_0 can be fitted by the starting position (see
248 Supplementary text). (**C**) Representative examples of single-cell trajectories (3
249 colors represent 3 different tracks) showed the reversion behavior of bacteria
250 around their mean positions.
251

252 To better understand how the spatial modulation of expected drift velocity
253 emerges, we adopted a one-dimensional minimal model of bacterial behavior.
254 The biased random motions of individual cells are described as an active
255 Brownian particle in the low Reynolds number regime in the medium, following a
256 Langevin type equation $dx_i = V_{D,i} dt + \epsilon dW$ (Berg, 2004). In the stochastic
257 velocity is modelled by a Gaussian random force ϵdW of which the variance
258 ϵ depends on the effective diffusion coefficient of the cells (Rosen, 1973, Rosen,
259 1974), while the deterministic velocity is the expected drifted velocity $V_D =$
260 $\chi g(x, t)$ that depends on two key parameters (Celani & Vergassola, 2010, de
261 Gennes, 2004, Dufour et al., 2014, Si et al., 2012): the cell chemotactic ability, χ,
262 and the perceived attractant gradient $g(x, t)$ (Eq. S3). To calculate the perceived
263 attractant gradient, we considered the dynamics of attractant concentration
264 $S(x, t)$ as a diffusible small molecule that can be consumed by the cells (Eq. S2).
265 Such stochastic description is equivalent to the classic Keller-Segel model (Keller
266 & Segel, 1971, Rosen, 1973). For simplicity, we considered each cell has the
267 same attractant consumption rate independent to the local cell density, and
268 omitted the hydrodynamic forces and physical interactions among cells
269 (Drescher, Dunkel et al., 2011, Fu et al., 2018, Saragosti et al., 2011). Using this
270 particle-based model, 100,000 cells were simulated in one dimension. Starting
271 with all cells in one end ($x_i = 0$) and homogenously distributed attractant field
272 ($S(x) = S_0$), a stable band of cells would spontaneously emerge by following a
273 moving gradient of attractant that is generated by cell consumption for both
274 single phenotype and multi-phenotypes (Fig S4). In the presence of diversity in
275 cell chemotactic ability, the traveling band exhibits a sorted structure of
276 phenotypes as previously observed (Fu et al., 2018). The self-generated
277 perceived attractant gradient in the moving coordinate, $g(z)$, exhibits a stable
278 profile that decreases from back to front.

279 In the moving coordinate, the Langevin type equation writes: $dz_i = V_{D,i} dt -$
280 $V_G dt + \epsilon dW$. It tells us that the motion of each individual cell relative to the group
281 migration can be considered as an active particle regulated by two 'effective
282 forces': one generated by the decreasing trend of V_D which pushes the cell to
283 catch up the wave; and another generated by the moving gradient of V_G which
284 leaves the cell fall behind the wave. This mechanism constrains the random
285 motions of cells, and enable cells with different phenotypes to form the spatially
286 ordered structure spontaneously. Specifically, for cells with chemotactic ability χ_i,

287 the balance between the two 'effective forces' produces an effective potential
288 well $U(z) \propto \int_z^{+\infty} V_{D,i}(z)dz$ (Eq. S17).

289 The simulation results (Fig S4F) show that the perceived gradient $g(z)$ is almost
290 linear along the band profile. Thus, we further approximated $g(z)$ as a linear
291 function of z around the peak position: $g(z) \approx g_0 + g_1 z$ with $g_1 < 0$, which gives
292 us an analogy that cells follow an Ornstein-Uhlenbeck (OU) type process in the
293 moving coordinate $dz_i = \chi_i g_1 z dt + (\chi_i g_0 - V_G)dt + \epsilon dW$. Solving this equation,
294 we obtained that cells perform mean reversion motions around the mean
295 positions $z_0 = -\frac{g_0}{g_1} - \frac{V_g}{\chi_i |g_1|}$ with the reversion rate $r = \left| \frac{dV_D(z)}{dz} \right| = \chi_i |g_1|$ (see
296 Supplementary text). As a result, the run-and-tumble random motions of cells are
297 constrained in the potential well, of which the minimum (the same as the mean
298 position of cells, z_0) increases with the chemotactic ability of the cells χ_i. In
299 addition, the standard deviation (σ) of spatial distributions of cells, given by
300 $\sigma = \frac{\epsilon}{\sqrt{2\chi_i |g_1|}}$, decreases with χ_i.

301 This analysis suggests that the spatial ordering of cells does not care how is the
302 perceived moving gradient $g(z)$ is generated, as long as the slope of it $g_1 < 0$ is
303 negative. Thus, we deduced a non-consumable moving attractant field ($S(z)$)
304 from the measured density profile $\rho(z)$ (Eq. S12), and simulated the behavior of
305 cells following the Langevin type equation under this moving attractant field. As
306 shown in Fig S5, cells with large enough χ follows the moving attractant field and
307 are spatially sorted as predicted by the OU type model.
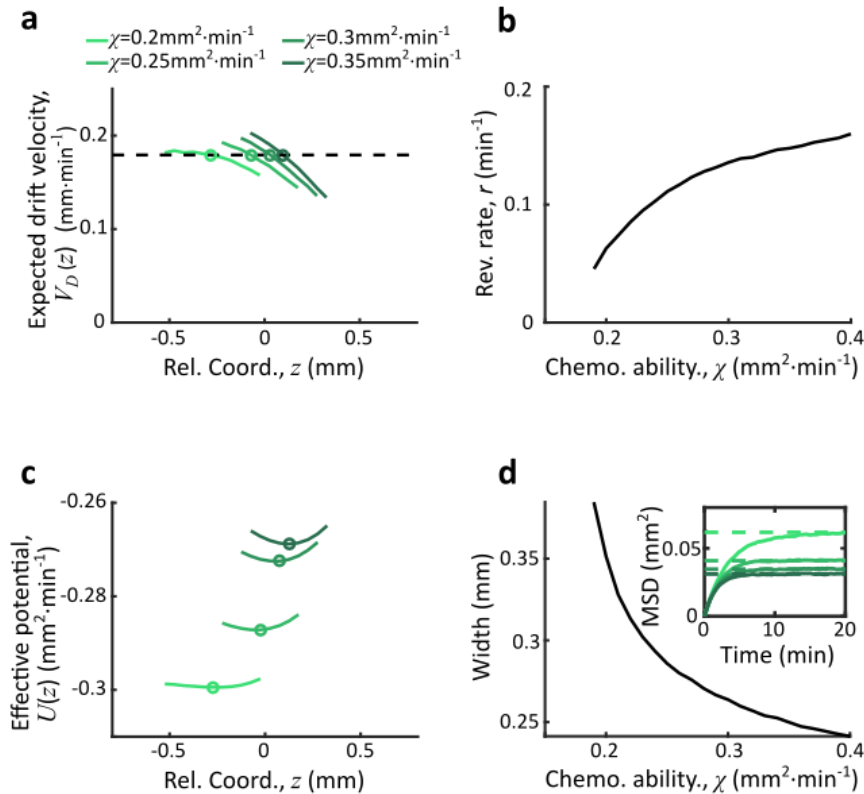
Figure 3. Agent-based simulations recapture the ordered structure of bacterial motions.

(**A**) The expected drift velocity $V_D(z)$ of simulated bacteria decreases from the back to the front of the migration group, where the chemotactic ability χ ranges from 0.2 to 0.35 $mm^2 \cdot min^{-1}$, consistent with the experimental results shown in Fig. 2a. The intersections between V_D curves with the preset group velocity V_G (black dashed line) shifts towards the back of the migration group as χ decreases (circles). Different colors of the lines and circles correspond to different chemotactic abilities χ as shown in the legend. The same color-coding also applies to (**B-D**). (**B**) The reversion rate $r_i = |dV_{D,i}(z)/dz|$ increases with the chemotactic ability. (**C**) The effective potential well calculated by $U_i(z) = \int_z^{+\infty} V_{d,i}(z)dz$. Positions of the potential minimum z_{min} are marked as circles. As illustrated, for a lower chemotaxis ability χ, the potential well is shallower and z_{min} shifts towards the back part of the migration group. (**D**) The width of the density profile (measured by 2σ, see Fig. 1B) decreases with the reversion rate r_i as well as the chemotaxis ability χ_i. The mean square displacement (MSD) of bacteria (insert, solid lines) is bounded to $2\sigma_i^2$ (insert, dash lines) (see Supplementary text). In panel (**A, C**), curves were cut to present 90% majority of cells ($z_{min} \pm 1.65\sigma_i$). More details of this simulation results were presented in Fig. S7.

**Ordered effective potential wells for bacteria of different phenotypes.**

To consolidate the proposed mechanism underlying the emergence of spatial orders from the individual random motions, we further performed simulations for cells of various chemotactic abilities integrated with the chemotactic pathway and multi-flagella competition. Together with the attractant dynamics $S(x,t)$ described in Eq. S2, we performed stochastic simulations in three dimensions of a population with different chemotactic abilities χ_i, where χ_i was varied by tuning the receptor gain N (For details in Supplementary text)(Dufour et al., 2014, Jiang, Qi et al., 2010, Sneddon, Pontius et al., 2012). As the receptor gain only affects the amplification factor that a cell responds to the gradient, the variation of bacterial motility ϵ is unchanged. As a result, a dense band of migrating cells that follow a self-generated moving attractant chemoattractant gradient via consumption were recaptured as experiments (Fig S6). To better analysis the simulations, we then simplified the model by the assumption of a non-consumable attractant profile $S(z)$ moving along the group migration direction (Fig S5A). Using this simplified model, we first checked that mean positions of density profiles of cells with different receptor gain N, as well as their peaks, were orderly aligned in respect to chemotactic ability χ_i.

As an important advantage of the agent-based simulations, the model allows us to analyze the single cell behavior during the ordered group migrations. For each phenotype i, the expected drift velocity $V_{D,i}(z)$ decreases along the density profile (Fig 3A). Consistent with the ordered structure of density profiles, the intersection between $V_{D,i}(z)$ and V_G exhibits the same sorted order of chemotactic ability χ_i (Fig S7). As the reversion rate $r_i = \left|\frac{dV_{D,i}(z)}{dz}\right|$ shows a positive correlation to χ_i, cells with lower receptor gain N (resulting smaller χ) experience a weaker reverting force towards centers (Fig 3B). Thus, the effective moving potential, $U_i(z)$, which constrains the cells round mean positions sorted by their chemotactic abilities, becomes flat for cells with lower chemotaxis ability χ (Fig 3C) (Long, 2019). As a result, cells of each phenotype perform as sub-diffusion, of which the MSD along the migration coordinate relative to the group are bounded at the level negatively correlated to χ (Fig 3D). We further obtain similar results for populations of different χ_i through adaptation time τ, or basal CheY protein level Y_{p0} which determines the basic tumble bias TB_0 (Dufour et al., 2014, Jiang et al., 2010, Sneddon et al., 2012) (Fig S8).

To verify the model predictions on the individual behavior of different phenotypes, we experimentally measured the trajectories of cells with different chemotactic abilities during the group migration. Specifically, we altered the chemotaxis abilities of cells by titrating the expression level of Tar, which is under the control of a small molecule inducer aTc (Sourjik & Berg, 2004, Zheng, Ho et al., 2016) (see Materials and Methods and Fig 4A). The variations on the expression of Tar would lead different receptor gains in response to the Asp gradient (Adler, 1966b,

370   Adler, 1969, Tu, 2013), but the tumble bias and growth rate will not change (Fig
371   S9). The tar-titrated cells labeled with yellow fluorescent protein (strain JCY20),
372   were added into wild type population by the ratio of 1 in 400. Within the wild type
373   population, 1 in 50 cells were labeled with red fluorescent protein (strain JCY2).
374   As the tar-titrated strain is a small portion of the pre-mixed population, we can
375   consider the density profile of the population is invariant to different inductions of
376   tar. The premixed population can generate a collective group migration as the
377   wild type population does (Fig S9). The trajectories of YFP labeled cells were
378   tracked to represent the behavior of cells with different chemotactic abilities,
379   while the profile of wild type cells with RFP was also measured to characterize
380   the density distribution of the entire migratory population.

381   By comparing the statistics of cells with different Tar expression levels, we found
382   that the expected drift velocity $V_{D,i}(z)$ followed the same decreasing pattern from
383   back to front (Fig 4B). More importantly, as the Tar-level (chemotactic ability)
384   increases, the slope of the decreasing pattern increases, which is consistent to
385   the model prediction shown in Fig 3A. The intersections between $V_{D,i}(z)$ and V_G,
386   as well as the peak positions and mean positions of each tar-titrated density
387   profiles (Fig 4C), shift toward the front as the chemotactic ability increases
388   (measured by migration rate on agar plate (Cremer et al., 2019, Liu, Cremer et
389   al., 2019)). The V_D cross point is always behind the peak position and the mean
390   position (Fig 4C), suggesting that cells are leaking behind. Moreover, the width of
391   each tar-titrated density profile (defined by $2\sigma_i$) decreases as the reversion rate r_i
392   increases (Fig 4D), consistent with the model results in Fig 3C. Thus, as the O-U
393   type model predicts, the width of the density profile is controlled by the reversion
394   rate determined by the chemotactic ability χ_i.
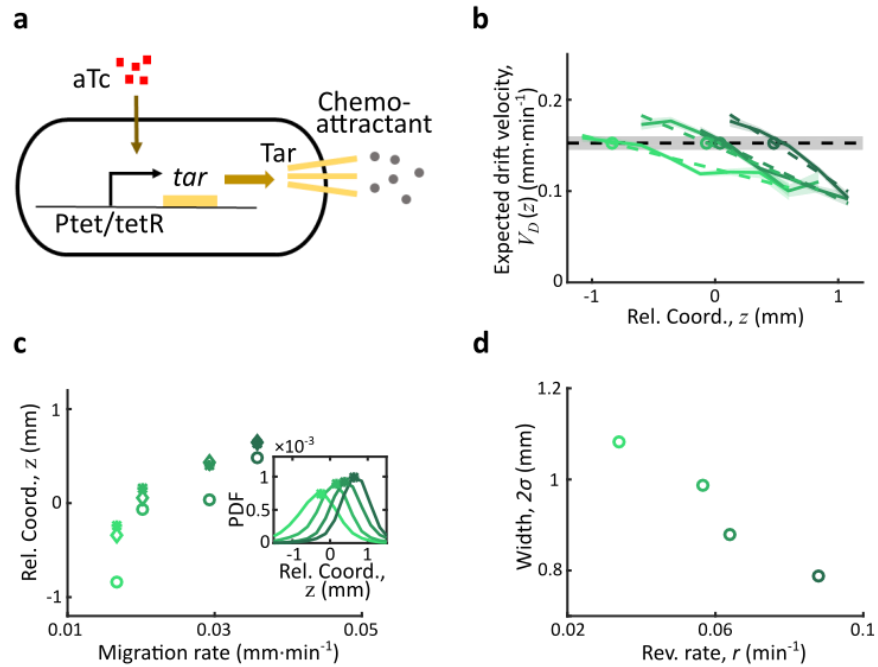
Figure 4. Spatial ordered structure emerged from behavioral modulation of cells with different chemoreceptors.

(**A**) Genetic circuit of the Tar titratable strain. In the experiments, the expression level of Tar (a chemo-attractant receptor protein) was titrated by the concentration of external inducer (aTc). The chemotactic ability χ of bacteria is then determined by the expression level of Tar (*41*). (**B**) The expected drift velocity $V_{D,i}(z)$ of Tar titratable strain JCY20 (colored solid line) were spatially modulated. All of them decrease from the back to the front of the migration group and intersect with the group migration velocity $V_G \approx 0.15 mm/min$ (black dash line). The linear fits of $V_{D,i}(z)$ (colored dash lines) intersect with V_G at positions (circles) determined by the corresponding Tar expression level. Colors from dark to light green corresponds to inducer (aTc) concentration to be $[1, 3, 6, 20] ng/mL$. The black shaded area of V_G represents s.d. of 4 experiments, while the colored shaded area of V_D curves presents s.e.m. of counted runs. (**C**) In the experiment, the positions of $V_{D,i}(z)$-V_G intersections (circles, illustrated in B), together with the peaks (stars, illustrated in the insert figure) and the average positions (diamond) of bacteria density profiles all shift towards the front of the migration group for strains with the higher Tar-expression level, which has a higher chemotactic ability and migrate faster on agar plates (x-axis, see Method & Fig. S9). The related density profiles (PDF) were shown in the insert plot and the color-coding of lines/symbols in both panel C and D is the same as that in B. (**D**) The width of density profiles (2σ) of Tar-titrated bacteria decreases with the reversion rate r.

14

Discussion

420

421 In summary, coordinated behaviors with ordered spatial arrangements of
422 phenotypes are abundant in a wide range of biological and human-engineered
423 systems and are believed to involved elaborate control mechanisms. For animal
424 migrations, it is challenging to characterize simultaneously the computational
425 strategy and behavior at individual levels so as to avoid averaging out phenotypic
426 diversity, and the emergent behavior at population level (Couzin et al., 2005,
427 Couzin et al., 2002, Vicsek & Zafeiris, 2012). Using bacterial chemotactic
428 migration as a model system, we demonstrate that individual bacteria can
429 spatially modulate their stochastic behaviors to perform mean reversion random
430 motions around centers sequentially aligned by their chemotactic abilities,
431 enabling a constant migration speed and ordered spatial arrangement of
432 phenotypes at the collective level. Individual cells harness their own chemotactic
433 system, together with collective consumption of attractant, to achieve the
434 behavioral modulation, such that system transits from solitary to collective
435 behaviors. This strategy of self-organization does not require sophisticated
436 communications (Curatolo, Zhou et al., 2020, Karig, Martini et al., 2018, Liu, Fu
437 et al., 2011, Payne, Li et al., 2013) nor other hydrodynamic interactions (Chen,
438 Liu et al., 2017, Drescher et al., 2011, Zhang, Be'er et al., 2010) among
439 individuals.

440 The behavior modulation depends on the chemotactic ability of individual, which
441 is controlled by well determined chemotaxis related proteins. Amount them, we
442 experimentally identified the abundance of the receptor protein Tar affects
443 linearly the reversion rate and the width of dispersion. Simulation results
444 suggests other key proteins that determines the basal tumble bias and the
445 adaptation time may also affect the behavior modulation (Fig S8).

446 In the migratory group, the same rule of behavioral modulation applies to cells
447 with different phenotypes, such that the random motions of cells are bounded by
448 moving potential wells whose basin are sequentially aligned. However, it is
449 noteworthy that cells could skip the potential wells from the back (Long, 2019),
450 resulting leakage of cells in the migratory group (Holz & Chen, 1978,
451 Novickcohen & Segel, 1984, Scribner, Segel et al., 1974). Phenotypes with
452 weaker chemotactic abilities locating at the back of the group, where the effective
453 potential well is shallower (Fig 3C), have more chance left to skip. Thus, such
454 collective migration selects bacteria with higher chemotactic abilities (Liu et al.,
455 2019).

456 The simple computational principle of behavioral modulation to allocate different
457 phenotypes in the collective group is likely not limited to sensing the self-
458 generated signal by consumption of attractant. Prominent example as trail-
459 following migration (Couzin & Krause, 2003, Helbing, Keltsch et al., 1997), a
460 typical class of collective behavior, a modified Langevin type model, where

15

461   individuals tracing the accumulated signal secreted by all participants (Eq. S20),
462   can reproduce similar spatiotemporal dynamics of behavioral modulation as well
463   as ordered arrangements of phenotypes in the migratory group (Fig S10). Thus,
464   this mechanism of matching individual abilities by the signal strength might
465   provide an explanation of how other higher organisms organize ordered
466   structures during group migration.

467

468   **Table 1. Summary of quantities**

Quantities	Definition	Formulations
V_G	Group velocity	$V_G = \langle \frac{dx}{dt} \rangle$
z	Moving coordinate	$z = x - V_G t$
$V_I(z)$	Instantaneous velocity	$V_I(z) = \langle \frac{dx(z)}{dt} \rangle$
$B_\tau(z)$	Run time bias	$B_\tau(z) = \frac{\langle \tau_R(z) \cdot cos\,\theta_R(z) \rangle}{\langle \tau_R(z) \rangle}$
$B_l(z)$	Run length bias	$B_l(z) = \frac{\langle l_R(z) \cdot cos\,\theta_R(z) \rangle}{\langle l_R(z) \rangle}$
$V_D(z)$	Expected drift velocity	$V_D(z) = \frac{\langle L_R(z) \cdot cos\,\theta_R(z) \rangle}{\langle \tau_R(z) + \tau_T(z) \rangle}$
$\rho(z)$	Cell density	$\rho(z) = \frac{\sum i(z)}{a \cdot \Delta z}$
$S(z)$	Chemo-attractant concentration	$-V_G \frac{dS}{dz} = D_s \frac{\partial^2 S}{\partial z^2} - k\rho$
$g(z)$	Perceived gradient	$g(z) = \frac{d\,ln\left(\frac{1+S(z)/K_{off}}{1+S(z)/K_{on}}\right)}{dz}$

469

Materials and Methods

Strains

The wild type strain *Escherichia coli* (RP437) and its mutants used in this study were used in this study, where all plasmids were kindly provided by Dr. Chenli Liu. Specifically, the tar-titratable strain was constructed by recombineering according to a previous research (Zheng et al., 2016). Specifically, the DNA cassette of the *Ptet-tetR-tar* feedback loop was amplified and inserted into the chromosomal *attB* site by recombineering with the aid of plasmid *pSim5*. The *tar* gene at the native locus was seamlessly replaced with the *aph* gene by using the same recombineering protocol. To color-code the strains, we use plasmids with chloramphenicol resistant gene carrying YFP under constitutive promoter (for JCY1 strain) and *pLambda* drived mRFP1 plasmids maintained by kanamycin (For JCY2). To color-code tar-titratable strain (JCY20), a plasmid carrying YFP chloramphenicol resistant gene were transformed into constructedtar-titratable strain.

Media and growth conditions

For bacterial culture, the M9 supplemented medium was used. The preparation of the M9 supplemented medium follows the recipe in previous study (Fu et al., 2018): $1\times$M9 salts, supplemented with 0.4% (v/v) glycerol, 0.1% (w/v) casamino acids, 1.0mM magnesium sulfate, and 0.05% (w/v) polyvinylpyrrolidone-40. $1\times$M9 salts were prepared to be $5\times$M9 salts stock solution: $33.9\mathrm{g}\cdot\mathrm{L}^{-1}$ Na_2HPO_4, $15\mathrm{g}\cdot\mathrm{L}^{-1}$ KH_2PO_4, $2.5\mathrm{g}\cdot\mathrm{L}^{-1}$ NaCl, $5.0\mathrm{g}\cdot\mathrm{L}^{-1}$ NH4Cl.

For migration experiments in the micro-channel, the M9 motility buffer was used. The recipe was: $1\times$M9 salts, supplemented with 0.4% (v/v) glycerol, 1.0mM magnesium sulfate, and 0.05% (w/v) polyvinylpyrrolidone-40, 0.1mM EDTA, 0.01mM Methionine, and supplemented with 200μM aspartic acid.

For the migration rate measurements, the M9 amino acid medium with 0.2% (w/v) agar was used to prepare swim plate(Liu et al., 2019). The recipe was: $1\times$M9 salts, supplemented with 0.4% (v/v) glycerol, $1\times$ animo acid, 200μM aspartic acid, 1.0mM magnesium sulfate, and 0.05% (w/v) polyvinylpyrrolidone-40. $1\times$ animo acid were prepared to be $5\times$ animo acid stock solution: 4mM alanine, 26mM arginine (HCl), 0.5mM cysteine ($HCl\cdot H_2O$), 3.3mM glutamic acid(K salt), 3mM glutamine, 4mM glycine, 1mM histidine ($HCl\cdot H_2O$), 2mM isoleucine, 4mM leucine, 2mM lysine, 1mM methionine, 2mM phenylalanine, 2mM proline, 2mM threonine, 0.5mM tryptophane, 1mM tyrosine, 3mM valine. All experiments were carried out at 30 °C. Plasmids were maintained by $50\,\mu\mathrm{g}\cdot\mathrm{mL}^{-1}$ kanamycin or $25\,\mu\mathrm{g}\cdot\mathrm{mL}^{-1}$ chloramphenicol.

Sample preparation

17

508 The bacteria from frozen stock was streaked onto the standard Luria-Bertani (LB)
509 agar plate with 2% (w/v) agar and cultured at 37°C overnight. 3-5 separate
510 colonies were picked and inoculated in 2mL M9 supplemented medium for
511 overnight culture with corresponded antibiotics to maintain plasmids. The
512 overnight culture was diluted by 1:100 into 2mL M9 supplemented medium the
513 next morning. For Tar titration strains, related aTc were added in this step. When
514 the culture OD600 reaches 0.2-0.25, it was then diluted into pre-warmed 15mL
515 M9 supplemented medium so that the final OD600 was about 0.05 (Liu et al.,
516 2019, Zheng, Bai et al., 2020, Zheng et al., 2016).

517 Bacteria were washed with the M9 motility buffer and were re-suspended in fresh
518 M9 motility buffer to concentrate cell density at OD600 about 1.0. Then, the wild
519 type strain and fluorescent strain were mixed with ratio of 400:1 before loaded in
520 the microfluidic chamber (Fu et al., 2018, Saragosti et al., 2011). For Tar titration
521 experiments, the wild type strain (RP437) was mixed with two fluorescent strains
522 (JCY2 & JCY20) by 400:8:1.

Microfabrication

524 The microfluidic devices were fabricated with the same protocol and the same
525 design as previous research (Bai, Gao et al., 2018, Fu et al., 2018), except that
526 the capillary channel was designed longer than that of previous ones. The size of
527 the main channel was $20\text{mm} \times 0.6\text{mm} \times 0.02\text{mm}$ and only one gate at the end of
528 the channel was kept (Fig S1A).

Band formation

530 Sample of mixed cells with density OD600 ≈ 1.0 was gently loaded into the
531 microfluidic device and then the device was spun for 15min at $3000rpm$ in an
532 $30\,°\text{C}$ environmental room so that almost $1{\sim}1.5 \cdot 10^5$ cells were placed to the end
533 of the channel. After spinning, the microfluidic device was placed on an inverted
534 microscope (Nikon Ti-E) equipped with a custom environmental chamber set to
535 50% humidity and $30\,°\text{C}$.

Imaging

537 The microscope and its automated stage were controlled by a custom MATLAB
538 script via the μManager interface (Edelstein, Tsuchida et al., 2014, Fu et al.,
539 2018). A 4X objective (Nikon CFI Plan Fluor DL4X F, N.A. 0.13, W.D. 16.4 mm,
540 PhL) was placed in the wave front and the fluorescent bacteria, seen as
541 randomly picked samples of the migrating group, were captured continuously in
542 10 mins until they leave the view. Time-lapsed images with YFP fluorescence of
543 the migrating cells were acquired by a ZYLA 4.2MP Plus CL10 camera ($2048 \times$
544 2048 array of $6.5 \times 6.5\,\mu m$ pixels) at 9 frames/s (fps) through. A LED illuminator

18

545 (0034R-X-Cite 110LED) and an EYFP block (Chroma 49003; Ex: ET500/X 20,
546 Em: ET535/30 m) compose the lightening system.

547 For the Tar titration experiments, the channel was first scanned with 10X
548 objective (CFI Plan Fluor DL 10X A, N.A. 0.30, W.D. 15.2mm, PH-1) enlighten by
549 a LED illuminator (0034R-X-Cite 110LED) through the RFP block (Chroma
550 49005, Ex: ET545/X 30, Em: ET620/60 m) and EYFP block channels for 7
551 neighbored views around the migration group. These images were further
552 combined to 2 large pictures of the RFP fluorescent strains and YFP fluorescent
553 strains. The channel was scanned twice, respectively before and after the 10
554 mins tracking of fluorescent Tar titrated cells.

Tracks extraction and state assignment

556 The acquired movie was first analyzed with the U-track software package to
557 identify bacteria and to get their trajectories (Jaqaman, Loerke et al., 2008). Then
558 the tracks were labeled by run state and tumble state by a custom MATLAB
559 package (Waite et al., 2016) using a previously described clustering algorithm
560 (Dufour et al., 2016).

Track analysis

562 The group velocity V_G was calculated by averaging the frame to frame velocity
563 ($dt \approx 0.11s$) over all tracks and all time. The cell number for the first frame over a
564 spatial bin of $\Delta x = 60\mu m$ and a channel section $a = 12000\mu m^2$ were calculated to
565 get the density profile $\rho(x, t = 0) = \frac{\Sigma i(x,t)}{a \cdot dx}$. The peak position of the first frame
566 ($x_{peak}(t = 0)$) was then determined by the maximum of $\rho(x, t = 0)$. The position
567 of each bacterium ($x_i(t)$) was transformed to moving coordinate position z_i by the
568 group velocity V_G and origin of the axis on the density peak by $z_i = x_i(t) - V_G t -$
569 $x_{peak}(t = 0)$. Given the relative position of each cell, we recalculated the density
570 profile in moving coordinate $\rho(z) = \frac{\Sigma i(z)}{a \cdot dx}$. The width of the density profile was
571 defined by two times the standard deviation of relative positions $2\sigma =$
572 $2\sqrt{\frac{1}{n-1}\sum_{i=1}^{n}(z_i - \langle z \rangle)^2}$. The spatial distribution of the instantaneous velocities
573 $\langle V_I(z) \rangle$ were calculated by averaging the velocity in spatial bin of $\Delta z = 240\mu m$.

574 A tumble-run event is the minimal element of bacterial behavior. The typical
575 spatial scale of a tumble-run event is about 20μm, which is much smaller than
576 the spatial bin size chosen in this study (240μm). The spatial distributions of run
577 time $\langle \tau_R(z) \rangle$, tumble time $\langle \tau_T(z) \rangle$ and run length $\langle l_R(z) \rangle$ were calculated by
578 averaging the related values of all the events with tumbling position (z_T) located
579 in each spatial bin (z). As the displacement of tumble is small, the tumbling
580 position is approximately the starting position of runs. For each tumble-run event,

19

we have the vector linking starting position and end position of the run. The running angle θ_R is then defined by the angle between run direction and the group migration direction. One can easily deduce all the other quantities with the formulations in Table 1.

Growth rate and migration rate measurement

Growth rates of Tar-titrated strains were calculated from exponential fitting ($R^2 > 0.99$) over measured curves of cell density (OD600) with respect to time. A $250\,\text{mL}$ flask with $20\,\text{mL}$ M9 supplement medium were used. All measurements were performed in a vibrator of rotation rate of $150\,\text{rpm}$ at $30℃$. OD600 was measured by a spectrophotometer reader every $25\,\text{min}$. Each strain has been measured for at least three times.

The semi-solid agar plate was illuminated from bottom by a circular white LED array with a light box as described previously (Liu et al., 2011, Liu et al., 2019, Wolfe & Berg, 1989) and was imaged at each 2 hours by a camera located on the top. As bacteria swimming in the plate forms 'Adler ring', we used the first maximal cell density from the edge to define the moving edge of bacterial chemotaxis. The migration rate was then calculated from a linear fit over the data of edge positions in respect to time ($R^2 > 0.99$).

Models and simulations

Details of the theoretical models and numerical simulations were presented in the appendix notes. In which, the Langevin equation was deduced and solved numerically with a particle-based simulation; the approximated OU type equation and its traveling wave solution was deduced; an agent-based simulation of bacterial with chemotaxis pathway was performed.

Acknowledgments

Author contributions: X.F. initiated and directed the research. C.H. constructed strains, fabricated micro-fluidics and tracked bacterial motions. Y.B. analyzed data, performed the particle-based simulations and the agent-based simulations. Y.B., X.L., and X.F. analyzed the results and mathematical modelling. All authors contribute in writing the manuscript.

Competing interests: The authors declare no competing interests.

Data and materials availability: All data needed to evaluate the conclusions in the paper are present in the paper and/or the Supplementary Materials. Codes for bacterial tracking and agent-based simulation were presented in previous papers and were modified with details presented in the Appendix. The OU model were simulated with Matlab and related codes were avablable on line: https://github.com/BaiYangBqdq/spatial_modulation_in_group_migration

References

Adler J (1966a) Chemotaxis in Bacteria. Science 153: 708-716

Adler J (1966b) Effect of Amino Acids and Oxygen on Chemotaxis in Escherichia Coli. J Bacteriol 92: 121-129

Adler J (1969) Chemoreceptors in bacteria. Science 166: 1588-97

Bai Y, Gao M, Wen L, He C, Chen Y, Liu C, Fu X, Huang S (2018) Applications of Microfluidics in Quantitative Biology. Biotechnol J 13: e1700170

Berg HC (2004) E. coli in motion. Springer-Verlag, New York

Berg HC, Brown DA (1972) Chemotaxis in Escherichia coli analysed by three-dimensional tracking. Nature 239: 500-4

Celani A, Vergassola M (2010) Bacterial strategies for chemotaxis response. P Natl Acad Sci USA 107: 1391-1396

Chen C, Liu S, Shi XQ, Chate H, Wu YL (2017) Weak synchronization and large-scale collective oscillation in dense bacterial suspensions. Nature 542: 210-214

Couzin ID, Krause J (2003) Self-organization and collective behavior in vertebrates. Adv Stud Behav 32: 1-75

Couzin ID, Krause J, Franks NR, Levin SA (2005) Effective leadership and decision-making in animal groups on the move. Nature 433: 513-516

Couzin ID, Krausew J, James R, D.Ruxton G, Franks NR (2002) Collective Memory and Spatial Sorting in Animal Groups. J theor Biol 218: 1--11

Cremer J, Honda T, Tang Y, Wong-Ng J, Vergassola M, Hwa T (2019) Chemotaxis as a navigation strategy to boost range expansion. Nature 575: 658-663

Curatolo AI, Zhou N, Zhao Y, Liu C, Daerr A, Tailleur J, Huang J (2020) Cooperative pattern formation in multi-component bacterial systems through reciprocal motility regulation. Nature Physics

de Gennes PG (2004) Chemotaxis: the role of internal delays. Eur Biophys J 33: 691-3

Drescher K, Dunkel J, Cisneros LH, Ganguly S, Goldstein RE (2011) Fluid dynamics and noise in bacterial cell-cell and cell-surface scattering. Proc Natl Acad Sci U S A 108: 10940-10945

Dufour YS, Fu X, Hernandez-Nunez L, Emonet T (2014) Limits of Feedback Control in Bacterial Chemotaxis. PLoS Computational Biology 10

Dufour YS, Gillet S, Frankel NW, Weibel DB, Emonet T (2016) Direct Correlation between Motile Behavior and Protein Abundance in Single Cells. Plos Computational Biology 12

Edelstein AD, Tsuchida MA, Amodaj N, Pinkard H, Vale RD, Stuurman N (2014) Advanced methods of microscope control using muManager software. J Biol Methods 1

Frankel NW, Pontius W, Dufour YS, Long J, Hernandez-Nunez L, Emonet T (2014) Adaptability of non-genetic diversity in bacterial chemotaxis. Elife 3

675 Fu X, Kato S, Long J, Mattingly HH, He C, Vural DC, Zucker SW, Emonet T
676   (2018) Spatial self-organization resolves conflicts between individuality and
677   collective migration. Nat Commun 9: 1-12
678 Helbing D, Keltsch J, Molnar P (1997) Modelling the evolution of human trail
679   systems. Nature 388: 47-50
680 Holz M, Chen SH (1978) Quasi-Elastic Light-Scattering from Migrating
681   Chemotactic Bands of Escherichia-Coli. Biophys J 23: 15-31
682 Jaqaman K, Loerke D, Mettlen M, Kuwata H, Grinstein S, Schmid SL, Danuser G
683   (2008) Robust single-particle tracking in live-cell time-lapse sequences. Nat
684   Methods 5: 695-702
685 Jiang LL, Qi OY, Tu YH (2010) Quantitative Modeling of Escherichia coli
686   Chemotactic Motion in Environments Varying in Space and Time. Plos
687   Computational Biology 6
688 Karig D, Martini KM, Lu T, DeLateur NA, Goldenfeld N, Weiss R (2018)
689   Stochastic Turing patterns in a synthetic bacterial population. Proc Natl Acad
690   Sci U S A 115: 6572-6577
691 Keller EF, Segel LA (1971) Model for chemotaxis. Journal of Theoretical Biology
692   30: 225-234
693 Krause J (1994) Differential fitness returns in relation to spatial position in
694   groups. Biol Rev Camb Philos Soc 69: 187-206
695 Krause J, Ruxton GD, Ruxton G, Ruxton IG (2002) Living in Groups. Oxford
696   University Press,
697 Kussell E, Leibler S (2005) Phenotypic diversity, population growth, and
698   information in fluctuating environments. Science 309: 2075-2078
699 Liu C, Fu X, Liu L, Ren X, Chau CK, Li S, Xiang L, Zeng H, Chen G, Tang LH,
700   Lenz P, Cui X, Huang W, Hwa T, Huang JD (2011) Sequential establishment
701   of stripe patterns in an expanding cell population. Science 334: 238-41
702 Liu WR, Cremer J, Li DJ, Hwa T, Liu CL (2019) An evolutionarily stable strategy
703   to colonize spatially extended habitats. Nature 575: 664-668
704 Long J (2019) From Individual to Collective Behavior: The Role of Memory and
705   Diversity in Bacterial Navigation. In Yale University
706 Long J, Zucker SW, Emonet T (2017) Feedback between motion and sensation
707   provides nonlinear boost in run-and-tumble navigation. PLoS Computational
708   Biology 13: 1-25
709 Novickcohen A, Segel LA (1984) A Gradually Slowing Traveling Band of
710   Chemotactic Bacteria. J Math Biol 19: 125-132
711 Parrish JK, Edelstein-Keshet L (1999) Complexity, pattern, and evolutionary
712   trade-offs in animal aggregation. Science 284: 99-101
713 Partridge BL (1982) The structure and function of fish schools. Sci Am 246: 114-
714   23
715 Payne S, Li B, Cao Y, Schaeffer D, Ryser MD, You L (2013) Temporal control of
716   self-organized pattern formation without morphogen gradients in bacteria.
717   Mol Syst Biol 9: 697
718 Rosen G (1973) Fundamental theoretical aspects of bacterial chemotaxis.
719   Journal of Theoretical Biology 41: 201-208

Rosen G (1974) On the propagation theory for bands of chemotactic bacteria. Mathematical Biosciences 20: 185-189

Saragosti J, Calvez V, Bournaveas N, Perthame B, Buguin A, Silberzan P (2011) Directional persistence of chemotactic bacteria in a traveling concentration wave. Proc Natl Acad Sci U S A 108: 16235-40

Scribner TL, Segel LA, Rogers EH (1974) Numerical Study of Formation and Propagation of Travelling Bands of Chemotactic Bacteria. Journal of Theoretical Biology 46: 189-219

Shimizu TS, Tu Y, Berg HC (2010) A modular gradient- sensing network for chemotaxis in Escherichia coli revealed by responses to time- varying stimuli. Molecular systems biology 6: 382

Si G, Wu T, Qi O, Tu Y (2012) Pathway-based mean-field model for Escherichia coli chemotaxis. Physical Review Letters 109: 0-4

Sneddon MW, Pontius W, Emonet T (2012) Stochastic coordination of multiple actuators reduces latency and improves chemotactic response in bacteria. Proc Natl Acad Sci U S A 109: 805-810

Sourjik V, Berg HC (2004) Functional interactions between receptors in bacterial chemotaxis. Nature 428: 437-441

Spudich JL, Koshland DE (1976) Non-genetic individuality: Chance in the single cell. Nature 262: 467--471

Sumpter DJT (2010) Collective Animal Behavior. Princeton Univ. Press,

Tu Y (2013) Quantitative modeling of bacterial chemotaxis: signal amplification and accurate adaptation. Annu Rev Biophys 42: 337-59

Vicsek T, Zafeiris A (2012) Collective motion. Phys Rep 517: 71-140

Waite AJ, Frankel NW, Dufour YS, Johnston JF, Long J, Emonet T (2016) Non-genetic diversity modulates population performance. Molecular Systems Biology 12: 895

Waite AJ, Frankel NW, Emonet T (2018) Behavioral Variability and Phenotypic Diversity in Bacterial Chemotaxis. Annu Rev Biophys 47: 595-616

Wang F, Shi H, He R, Wang R, Zhang R, Yuan J (2017) Non-equilibrium effect in the allosteric regulation of the bacterial flagellar switch. Nature Physics 13: 710-714

Wolfe AJ, Berg HC (1989) Migration of Bacteria in Semisolid Agar. Proc Natl Acad Sci U S A 86: 6973-6977

Zhang HP, Be'er A, Florin EL, Swinney HL (2010) Collective motion and density fluctuations in bacterial colonies. Proc Natl Acad Sci U S A 107: 13626-13630

Zheng H, Bai Y, Jiang M, Tokuyasu TA, Huang X, Zhong F, Wu Y, Fu X, Kleckner N, Hwa T, Liu C (2020) General quantitative relations linking cell growth and the cell cycle in Escherichia coli. Nat Microbiol

Zheng H, Ho PY, Jiang M, Tang B, Liu W, Li D, Yu X, Kleckner NE, Amir A, Liu C (2016) Interrogating the Escherichia coli cell cycle by cell dimension perturbations. Proc Natl Acad Sci U S A 113: 15000-15005